**Naval Research Laboratory**

**Washington, DC 20375-5320**

**NRL/MR/6040--11-9354**

# Towards a Fast Dynamic Model of the Human Circulatory System

M.A. GREEN

*NAS/NRC Postdoctoral Research Associate*
*Laboratories for Computational Physics and Fluid Dynamics*

C.R. KAPLAN

*Laboratory for Propulsion, Energetic, and Dynamic Systems*
*Laboratories for Computational Physics and Fluid Dynamics*

J.P. BORIS
E.S. ORAN

*Laboratories for Computational Physics and Fluid Dynamics*

October 6, 2011

# REPORT DOCUMENTATION PAGE

*Form Approved*
*OMB No. 0704-0188*



| **1. REPORT DATE** *(DD-MM-YYYY)* | **2. REPORT TYPE** | **3. DATES COVERED** *(From - To)* |
|---|---|---|
| 06-10-2011 | Memorandum Report | |

**4. TITLE AND SUBTITLE**

Towards a Fast Dynamic Model of the Human Circulatory System

**5a. CONTRACT NUMBER**

**5b. GRANT NUMBER**

**5c. PROGRAM ELEMENT NUMBER**

**6. AUTHOR(S)**

M.A. Green,* C.R. Kaplan, J.P. Boris, and E.S. Oran

**5d. PROJECT NUMBER**

**5e. TASK NUMBER**

**5f. WORK UNIT NUMBER**
64-4464-01

**7. PERFORMING ORGANIZATION NAME(S) AND ADDRESS(ES)**

Naval Research Laboratory
4555 Overlook Avenue, SW
Washington, DC 20375-5344

**8. PERFORMING ORGANIZATION REPORT NUMBER**

NRL/MR/6040--11-9354

**9. SPONSORING / MONITORING AGENCY NAME(S) AND ADDRESS(ES)**

Office of Naval Research
One Liberty Center
875 North Randolph Street, Suite 1425
Arlington, VA 22203-1995

**10. SPONSOR / MONITOR'S ACRONYM(S)**

ONR

**11. SPONSOR / MONITOR'S REPORT NUMBER(S)**

**12. DISTRIBUTION / AVAILABILITY STATEMENT**

Approved for public release; distribution is unlimited.

**13. SUPPLEMENTARY NOTES**

*NRC Postdoctoral Research Associate

**14. ABSTRACT**

We describe a model for blood transport in the human circulatory system that is based on a set of equations for an unsteady elastic pipe-flow circuit. The Navier-Stokes equations are collapsed from three spatial dimensions and time to one spatial dimension and time by assuming axisymmetric vessel geometry and a parabolic velocity profile across the cylindrical vessels. Contractions of a beating heart that drive the fluid are modeled as prescribed area changes of the elastic vessels. When the effects of fluid acceleration are also included in the model equations, peak pressure increases and additional oscillations are introduced in local pressure and velocity. The model response to variations in the physical parameters and actuation are consistent with the human physiological response. Increasing the rigidity of the vasculature is found to increase peak arterial pressures on the order of 10%, and including a distributed vascular contraction to model distributed skeletal muscle contractions monotonically increases time-averaged blood flow in the veins. The computational model simulates the circulatory system on the order of one hundred times faster than real-time; that is, we compute thousands of heartbeats per minute, and time-resolved distributions of pressure, velocity, and area compare well with reference data.

**15. SUBJECT TERMS**

Circulatory system
Elastic pipe flow
Low-dimensional model

| **16. SECURITY CLASSIFICATION OF:** | | | **17. LIMITATION OF ABSTRACT** | **18. NUMBER OF PAGES** | **19a. NAME OF RESPONSIBLE PERSON** |
|---|---|---|---|---|---|
| **a. REPORT** | **b. ABSTRACT** | **c. THIS PAGE** | | | C.R. Kaplan |
| Unclassified | Unclassified | Unclassified | UU | 34 | **19b. TELEPHONE NUMBER** *(include area code)* (202) 767-2078 |

**Standard Form 298 (Rev. 8-98)**
**Prescribed by ANSI Std. Z39.18**

This page intentionally left blank.

# Contents

This page intentionally left blank.

# 1 Introduction

A truly detailed model of an entire human physiological system (circulatory, respiratory, etc.) is currently not feasible due to the complicated and dynamic geometry, multi-species and multiphase chemistry, and many complex biological processes on a wide range of spatial and temporal scales. To date, the main approach has been to create full scale, multi-dimensional, and detailed models of a limited section of a physiological system, such as the heart, a heart valve, or a section of vein or artery. These models obtain the high-fidelity solutions for a small part of the overall human system and help with local physiological diagnoses and treatments. Another approach, taken here, is to develop a broader and more integrated model that facilitates analysis of larger-scale material transport and response in the body and the diagnosis of time-dependent systems-level phenomena such as shock. This approach also provides a framework to integrate the calibrated submodels derived from detailed 3D simulations.

It is with these goals in mind that we develop a global, time dependent, yet low-dimensional fluid dynamics model of the human circulatory system. Development of this systems-level model is our first step of a larger effort to develop models of individual physiological systems and then to couple them together, while also permitting the use of both experimental data and more detailed simulations for calibration (Green *et al.*, 21-23 November, 2010; Staples *et al.*, 18-20 November, 2007). Each individual model will also allow for future extensions that can directly incorporate more branching networks or more detailed representations of the chemical or physical processes occurring. The goal of this larger effort is not to simulate details of individual systems, but to study the macro-system dynamics of the human body, as the effects of coupled interactions may be more important than the details of the individual physiological systems. We look to determine the necessary level of detail and accuracy in the submodels of an entire physiological system needed to reproduce observed behavior in realistic timeframes.

Most physiological systems in the human body, such as the circulatory, respiratory, and lymphatic systems, involve the transport of gases and liquids through elastic volumes and channels. They are, therefore, governed by the equations of reactive fluid dynamics. As a first step, we will consider a simplified model of the circulatory system, shown schematically in figure 1(a), as fluid circuits that incorporate blood flow in

Manuscript approved August 22, 2011.

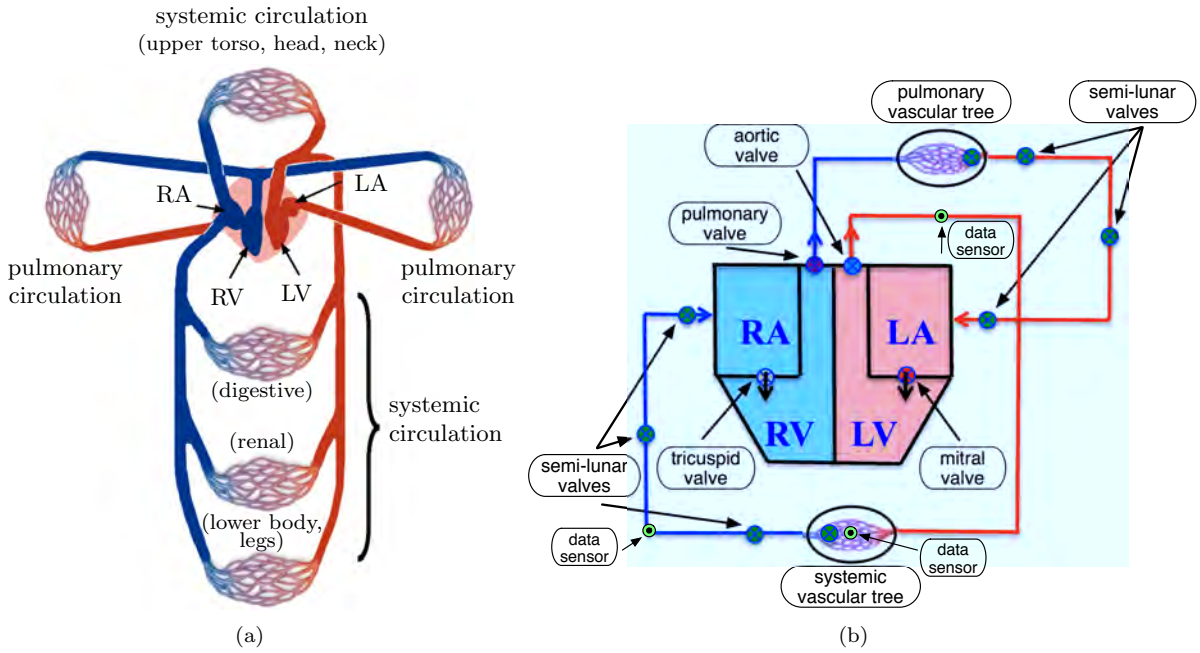


Figure 1: (a) Simplification of the circulatory system. (b) Diagram of our initial representation of the human circulatory system.

idealized flexible channels and chambers. The system shown in figure 1(b) is low-dimensional: three spatial dimensions are collapsed to one dimension with elastic cylindrical geometry. The description is dynamic and includes higher-dimensional effects such as boundary layers and the transition from convective to diffusive transport. This papers describes the relevant equations, the numerical schemes used to obtain fast and efficient simulations on a laptop computer, and benchmarks of the human circulatory system against which the model was compared.

## 2 Background

Many numerical models attempt to recreate the human circulatory system, ranging from detailed fluid-chemical simulations to lower-dimensional lumped parameter models. Our efforts parallel those that simulate biofluid flows with low-dimensional models. Among the first was Womersley, who studied the propagation of pressure waves in elastic cylinders as a model of arterial flow (Womersley, 1955, 1957). This work showed that for low forcing frequency, small radius, low viscosity, and low elasticity, it was adequate to assume that

the velocity profile was axisymmetric and parabolic. Since then, many efforts have used one-dimensional fluid equations to model the flow through large sections of the arterial system (Schaaf & Abbrecht, 1972; Zagzoule & Marc-Vergnes, 1986; Sheng *et al.*, 1995). In these cases, connected arterial segments were defined with assigned length, radius, and compliance. The one-dimensional flow through each of these segments was calculated using boundary conditions at branching locations that were determined using two principles: a conservation of mass as the vessels branched and pressure equivalence across the branching point.

The complexity of these models increases rapidly with the addition of more and smaller segments of the arterial tree. Olufsen *et al.* (2000) and Olufsen (1999) handled this by first calculating the flow through large arteries using the nonlinear Navier-Stokes equations, and then combining segments of smaller arteries together as a structured tree model governed by the linearized equations. This approach generated appropriate outflow boundary conditions for the nonlinear calculations in the large arteries, and the results compared favorably with experimental measurements.

Similarly, low-dimensional models of larger arterial geometries provided boundary conditions for more highly resolved computational simulations (Vignon-Clementel *et al.*, 2006). This approach also showed flow rates computed by the one-dimensional vascular models that compared well with fully resolved three-dimensional simulations and *in vivo* measurements (Steele *et al.*, 2003; Wan *et al.*, 2002). From the success of these results, the authors speculated that such low-dimensional models could be of direct medical use by providing a tool for real time surgery and therapy planning. Grinberg *et al.* (2009) performed a three-dimensional simulation of the circulation in the intracranial arterial system, and were also able to show good agreement in distributions of pressure and mass flow when compared against a simpler one-dimensional model (Grinberg *et al.*, 2011).

Low dimensional models have also been constructed using electrical circuit components, such as capacitors and resistors, to simulate the circulatory system dynamics (Noordergraaf *et al.*, 1963; Snyder *et al.*, 1968; Westerhof *et al.*, 1969). These circuit models used current to represent one-dimensional fluid flow and electric potential to represent the pressure differential along vessels. Electrical circuits were physically constructed as an "analog computer" that produced voltage and current data that compared well with measured

blood pressure and flow rates.

As an example of a comprehensive physiological that is not essentially based on the equations of fluid dynamics is the Physiome Project at the National Simulation Resource (NSR). The Physiome project is a collection chemical and biological models at a range of levels and an international effort to use them to create a full description of the human physiome (Neil & Bassingthwaighte, 2007; Bassingthwaighte, 2000). NSR has focused on creating open-source, user-friendly software and standard data formats, all of which encourages collaboration and modularization of the models available there.

Our circulatory system model is a closed circuit in which axisymmetric flow is pumped by a periodic contraction and relaxation of the heart chamber geometry. Prior models drove the fluid flow using prescribed boundary conditions on the pressure or velocity. Sheng *et al.* (1995) for example, provided the pulsatile aortic and constant caval (venous) pressures as inlet and outlet conditions of their model system. Other physiological phenomena, such as the implementation of valves to inhibit backflow in the heart chambers and the low-pressure venous system, and augmented blood pumping provided by the skeletal muscular system throughout the body, are also included in the development of our model circulatory system and differentiates our work from previous efforts.

# 3 The physical model

A diagram of the model circulatory system, figure 1(b), shows the four chambers of the heart: the right atrium and right ventricle (RA, RV), and the left atrium and left ventricle (LA, LV). There are four heart valves (mitral, aortic, tricuspid, and pulmonary) that control the flow through the heart and into the systemic and pulmonary systems. Semi-lunar valves in the vasculature prevent flow reversal which might occur due to the pulsatile nature of the heart pumping and resulting drops in pressure. The pulmonary and vascular trees, shown schematically on the top and bottom of the figure, are comprised of elastic vessels and contain much of the interesting physics of the problem. Here, the system branches form the large arteries into smaller arteries, into the smaller arterioles, and finally to the capillaries. To return to the heart, the capillary beds coalesce

into the ventrioles, collect into the smaller veins, and deposit into the large veins (inferior and superior vena cava). As the fluid moves back and forth between large vessels and smaller capillaries, the inherent flow physics change from being dominated by convective effects to being dominated by viscous effects.

Beginning at the left atrium of the heart (LA), oxygenated blood (red) is driven through the mitral valve into the left ventricle (LV), and then through the aortic valve into the systemic section of the circuit. When the flow enters the systemic vascular tree, the total cross sectional-area increases and there is a large pressure drop to drive the flow through the capillaries, where oxygen is delivered to organs, muscles, etc. After passing through the systemic vascular tree, the deoxygenated blood (blue) then passes through the venous system, and is drawn into into the right atrium. From here it is pumped through the tricuspid valve into the right ventricle, then through the pulmonary valve into the pulmonary vasculature, where a smaller yet comparable pressure drop drives the flow. Here, the pulmonary capillaries are intertwined with the small-scale alveoli of the pulmonary system, exchanging oxygen and carbon dioxide with the lungs. The oxygenated blood (red) is returned to the left atrium via the pulmonary veins, completing the circuit.

### 3.1 Flexible Flow Equations

The mathematical formulation for the flow is based on a solution of the Flexible Flow Equations (FFEs). Given appropriate initial and input conditions, the equations are solved for the pressure, velocity, and cross-sectional area of an incompressible flow as a function of time and position along a system of elastic channels. By assuming an axisymmetric parabolic velocity profile, the physical system collapses from three spatial dimensions and time to one spatial dimension and time.

The fluid velocity $u(S,t)$ at a distance $S$ along the loop and time $t$ is described by a momentum equation,

$$\frac{\partial u(S,t)}{\partial t} + u(S,t)\frac{\partial u(S,t)}{\partial S} = -\frac{1}{\rho}\frac{\partial p(S,t)}{\partial S} + \nu\frac{\partial^2 u(S,t)}{\partial S^2} - \frac{8\nu}{R(S,t)^2}u(S,t) + g(S,t), \tag{1}$$

where $\rho$ is the density, $\nu$ is kinematic viscosity, $R$ is the local radius of the pipe, $g$ is an external acceleration from gravity or any applied body force, and $p$ is the local pressure. Equation 1 satisfies the parabolic viscous

similarity solution with zero velocity at walls.

Because the fluid velocities are low compared to the speed of sound, we can assume that the fluid acceleration is small compared to the pressure gradient. Equation 1 is rearranged as,

$$\frac{8\pi\nu}{\pi R^2}u = -\frac{1}{\rho}\frac{\partial p}{\partial S} + g - \frac{\partial u}{\partial t} - u\frac{\partial u}{\partial S} + \nu\frac{\partial^2 u}{\partial S^2} = -\frac{1}{\rho}\frac{\partial p}{\partial S} + G(S,t), \tag{2}$$

where the generalized-acceleration term $G(S,t)$ is defined as,

$$G(S,t) \equiv g - \frac{\partial u}{\partial t} - u\frac{\partial u}{\partial S} + \nu\frac{\partial^2 u}{\partial S^2}. \tag{3}$$

In one limit, we can assume that $G = 0$, so that this acceleration is truly small compared to the pressure-gradient term. This, however, is generally not valid in the cases we are considering, where the acceleration can be large during fluid pumping. In §4 of this paper, when we present a solution method for the equations, we describe a method for including portions of the acceleration term. We also present and compare results for cases with $G = 0$ and $G \neq 0$.

Defining $A = \pi R^2$ and rearranging equation 2 gives,

$$u = \frac{AG}{8\pi\nu} - \frac{A}{8\pi\nu\rho}\frac{\partial p}{\partial S}. \tag{4}$$

Flexible walls are modeled by allowing the local area $A(S,t)$ to accommodate the local pressure through an equation of state,

$$p - p_{eq} = \frac{p_{eq}}{\varepsilon A_{eq}}\left(A - A_{eq}\right). \tag{5}$$

Here, $A_{eq}$ is the cross-sectional area of the the flexible channel at the equilibrium pressure $p_{eq}$, and $\varepsilon(S)$ is a dimensionless elasticity coefficient defined along the length of the channel. As the elasticity goes to zero (rigid walls), the area is pegged at the equilibrium area $A_{eq}$, independent of pressure changes. Note that $A_{eq}$ may be a function of $S$ and $t$, and is used in the model of the vascular trees as discussed below.

Even though the flow is incompressible, the local mass flow rate is not necessarily constant because the walls are elastic. The total mass of the fluid in the system remains constant, however, and therefore any local expansion must be balanced by contraction elsewhere. This is reflected in the continuity equation,

$$\frac{\partial A}{\partial t} = -\frac{\partial}{\partial S} uA. \tag{6}$$

Combining equations 5 and 6 yields the pressure equation,

$$\frac{\partial p}{\partial t} = \frac{p_{eq}}{\varepsilon A_{eq}} \frac{\partial A}{\partial t} = \frac{-p_{eq}}{\varepsilon A_{eq}} \frac{\partial (uA)}{\partial S} \ . \tag{7}$$

The term $uA$ can be obtained through equation 4,

$$uA = \frac{A^2 G}{8\pi\nu} - \frac{A^2}{8\pi\nu\rho} \frac{\partial p}{\partial S}. \tag{8}$$

Combining these equations, we arrive at a second-order diffusion equation for the pressure,

$$\frac{\partial p(S,t)}{\partial t} = \frac{p_{eq}}{\varepsilon(S) A_{eq}(S)} \frac{\partial}{\partial S} \left\{ \frac{A^2(S,t)}{8\pi\nu(S)\rho} \frac{\partial p(S,t)}{\partial S} \right\} - \frac{p_{eq}}{\varepsilon(S) A_{eq}(S)} \frac{\partial}{\partial S} \left\{ \frac{A^2(S,t) G(S,t)}{8\pi\nu(S)} \right\}. \tag{9}$$

### 3.2 Convective to diffusive flow in vascular trees

As the blood vessels branch in the systemic and pulmonary vascular trees, the total cross-sectional area increases rapidly and the flow rate drops correspondingly. Each vessel through which blood flows decreases in size, and therefore viscous effects become increasingly important. To address the transition from convective to diffusive flow in the systemic and pulmonary vascular trees, we define a weighted viscosity term, $\nu(S)$, that artificially increases in the small-scale capillary regions where the viscous term dominates despite the increasing $A$. The weighted viscosity is a smooth function that varies from a value of blood viscosity at the upstream and downstream ends of the vascular tree to a maximum value at the widest section of the vasculature representing the capillary bed, with the maximum value calibrated to reproduce a reasonable

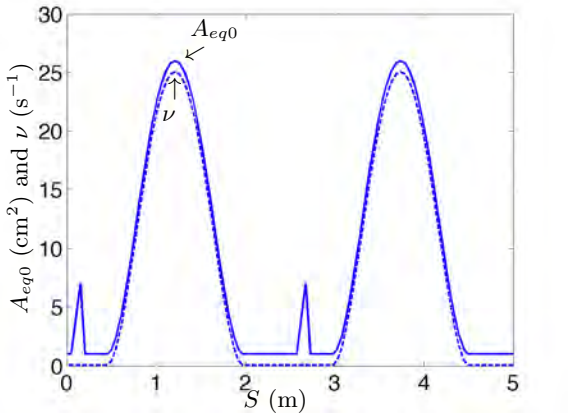


Figure 2: Area and viscosity along the length of the circulatory system.

pressure drop across the vascular tree. The weighted viscosity is written as,

$$\nu(S) = \nu_b \left(1 + \nu_{max} \frac{(S - S(X_1))(S(X_N) - S)^2}{(c(S(X_N) - S(X_1))^2)^2}\right) , \tag{10}$$

where $\nu_b$ is the blood viscosity, $c$ is a constant normalizing the distribution term to $\nu_{max}$ at the peak, and $S(X_1)$ and $S(X_N)$ are the locations of the upstream and downstream ends of a vascular tree.

The equilibrium area is initialized using a similar function to the viscosity in the vascular trees. The variation of both the equilibrium area and the viscosity along the length of the circulatory model are shown in figure 2. In this case, $X_1 = 0.5$m and $X_N = 2$m in for the systemic vascular tree, while $X_1 = 3$m and $X_N = 4.5$m for the pulmonary vascular tree. According to Guyton & Hall (2000), about 5 L is considered normal for an adult human, and the area distribution of our current model yields a total blood volume of 4.7 L. The distribution of weighted viscosity and equilibrium area across the model circulatory system is shown in figure 2.

### 3.3 Heart and skeletal muscle pumping

The blood flow is pumped by a prescribed periodic contraction and relaxation of the heart chambers, and the local time-varying pressure is not prescribed anywhere. The effects of muscle contraction and relaxation on the circulatory system are represented through imposed local changes in the equilibrium area. At each

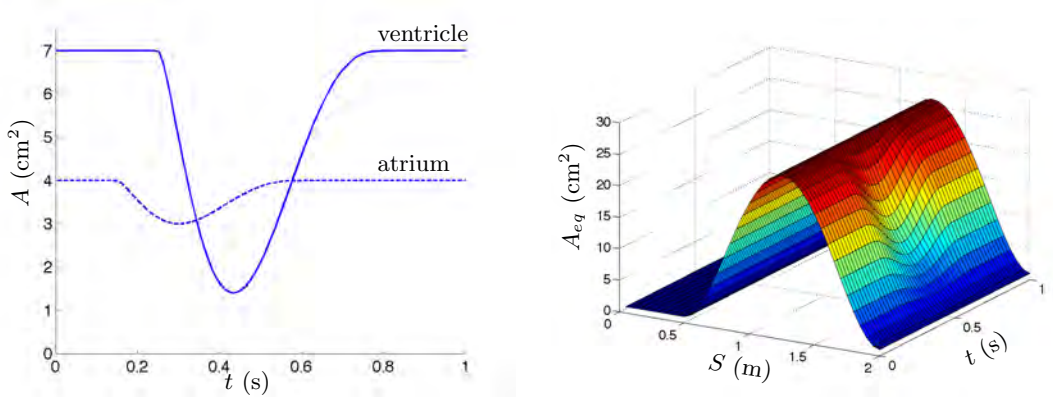


(a) (b)

Figure 3: (a) Cross-sectional area of the atria and ventricles during the period of one hearbeat. (b) Cross-sectional area of the vascular tree ($0.5 < S < 2$) area during skeletal muscle contraction. Contraction only applied on the venous end of the vascular tree ($1.25 < S < 2$). For the purposes of the visualization, the maximum amplitude of contraction is $\Delta A_m = 0.35$, and the frequency is 1 Hz.

location and time, $A_{eq}(S,t)$ is either increased or decreased to model a local relaxation or contraction of a muscle, respectively, and the local pressure is then adjusted accordingly. In the atria of the heart, for example, the contraction occurs for time ($t_{a1} < t < t_{a2}$), where ($t_{a2} - t_{a1} = T_a$) is the period of atria contraction. Similarly, $T_v$ is the period of ventricle contraction. The corresponding equilibrium area change in the atria is modeled as,

$$A_{eq}(S_a,t) = A_{eq0}(S_a)(1-\sigma(t)(1-\Delta A_a)), \quad \text{where}$$
$$\sigma(t) = \left[6.75\left(\frac{(t-t_{a1})(t_{a2}-t)^2}{(t_{a1}-t_{a2})^3}\right)\right]^{1.5}. \tag{11}$$

Here, $\Delta A_a$ is the fraction of the maximum area change during the atrial contraction ($\Delta A_v$ in the ventricles). The areas of the atria and ventricles in the heart, over the duration of one heartbeat, are shown in figure 3(a).

General systemic contractions of skeletal muscles are represented similarly. Small amplitude periodic, distributed contractions are applied to the venous side the systemic vascular tree ($S(X_{mid}) < S < S(X_N)$),

where $S(X_{mid}) = 0.5[S(X_1) + S(X_N)]$). Both the magnitude and the frequency are adjustable, so that

$$\begin{aligned}
\omega_{mt} &= \frac{2\pi t}{T_m} \\
\omega_{mx} &= \frac{2\pi(S - S(X_1))(S(X_N) - S)}{(S(X_N) - S(X_1))} \\
A_{eq} &= A_{eq0}\left(1 + \Delta A_m \cos(\omega_{mt})^2 \sin(\omega_{mx})\right),
\end{aligned} \tag{12}$$

where $T_m$ is the period of muscle contraction, occurring during time ($t_{am} < t < t_{bm}$), and $\Delta A_m$ is the maximum contraction amplitude. A visualization of the muscle contraction model is shown in figure 3(b).

Valves are an important part of the physical circulatory system to prevent flow reversal. This is necessary within the heart chambers, driving fluid out through the arteries instead of back through the atria and veins. In the low-pressure venous region, semi-lunar valves are also integral in directing blood back towards the heart by preventing backflow and pooling in the extremities. In the current work, both heart valves and venous semi-lunar valves are actuated in the same manner. At each valve location, the local pressure is monitored at every timestep. When an adverse pressure gradient is detected, the local area $A$ is initially decreased by 80%, and then to 0% at the next time step if the adverse pressure gradient persists.

# 4 Numerical Implementation

Figure 4 is a schematic of the layout of the computational domain based on Figure 1(b). Various regions of the circulatory system can be represented by an arbitrarily chosen number of computational cells, thus providing more or less resolution in those regions, as discussed in §5. This initial representation is a single loop, but the algorithm can be extended to treat different branches and sub-loops in a more complex network.

Equations 5, 8, and 9 are discretized to produce a tridiagonal system that can be solved iteratively at each time step. Equation 9 is discretized using a time derivative of pressure and a central spatial derivative

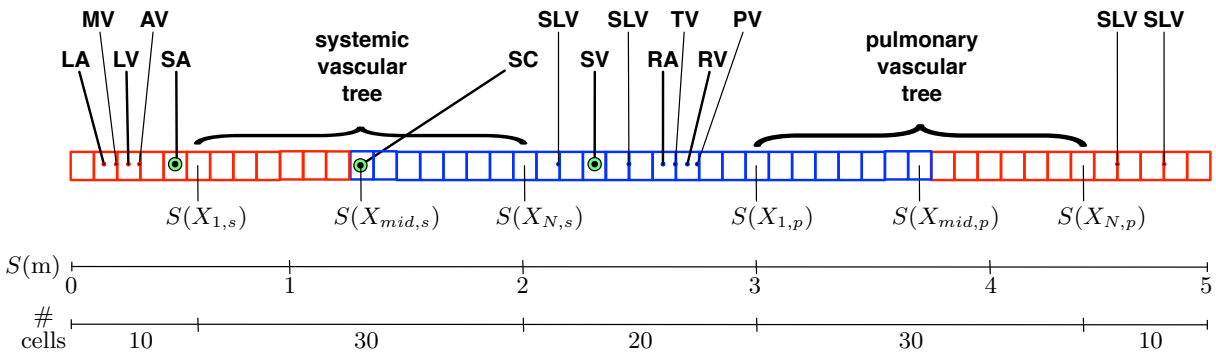


Figure 4: Diagram of the numerical implementation of the model. At top: LA, left atrium; MV, mitral valve; LV, left ventricle; AV, aortic valve; SLV, semi-lunar valves; RA, right atrium; TV, tricuspid valve; RV, right ventricle, and PV, pulmonary valve. Top scale line gives the dimensional distances, and the bottom scale line shows the distribution of computational cells for the baseline case, described in §5. Three cell-centered green targets indicate the approximate locations in the arteries (SA), the capillaries (SC), and the veins (SV), at which data is sampled in §5.

of a general variable $f$,

$$\frac{\partial p(S,t)}{\partial t} = \frac{1}{\delta t}(p^k - p^{k-1}) \qquad\qquad \frac{\partial f}{\partial S}_j = \frac{1}{\delta S_j}(f_{j+\frac{1}{2}} - f_{j-\frac{1}{2}}), \tag{13}$$

where $f$ can be any of the model quantities that vary in space ($f(S)$). The subscript $j$ indicates spatial indices in the range $[0,\ jN{+}1]$, where $N$ is the number of computational cells, and the superscripts $k$ and $k-1$ indicate the current and previous timestep, respectively. The areas and velocities are calculated at cell interfaces and at the half timestep, so that the time rate of change of pressure can be solved as a central difference.

Equation 9 then becomes

$$-\beta_j \alpha_{j-\frac{1}{2}} p^k_{j-1} + p^k_j \left\{1 + \beta_j(\alpha_{j+\frac{1}{2}} + \alpha_{j-\frac{1}{2}})\right\} - \beta_j \alpha_{j+\frac{1}{2}} p^k_{j+1} = p^{k-1}_j - \beta_j \left\{\gamma_{j+\frac{1}{2}} G_{j+\frac{1}{2}} - \gamma_{j-\frac{1}{2}} G_{j-\frac{1}{2}}\right\}, \tag{14}$$

where

$$\alpha_{j+\frac{1}{2}} = \frac{A^2_{j+\frac{1}{2}}}{8\pi\nu_{j+\frac{1}{2}}\rho\,\delta S_{j+\frac{1}{2}}}, \qquad \beta_j = \frac{\delta t\, p_{eq}}{\delta S_j \varepsilon_j A^{eq}_j}, \qquad \gamma_{j+\frac{1}{2}} = \frac{A^2_{j+\frac{1}{2}}}{8\pi\nu_{j+\frac{1}{2}}}. \tag{15}$$

Equation 14 is arranged into a tridiagonal system,

$$\mathbf{A}_j p_{j-1}^k + \mathbf{B}_j p_j^k + \mathbf{C}_j p_{j+1}^k = \mathbf{D}_j \tag{16}$$

with vector coefficients,

$$\begin{aligned}
\mathbf{A}_j &= -\beta_j \alpha_{j-\frac{1}{2}} \\
\mathbf{B}_j &= 1 + \beta_j (\alpha_{j+\frac{1}{2}} + \alpha_{j-\frac{1}{2}}) \\
\mathbf{C}_j &= -\beta_j \alpha_{j+\frac{1}{2}} \\
\mathbf{D}_j &= p_j^{k-1} - \beta_j \left( \gamma_{j+\frac{1}{2}} G_{j+\frac{1}{2}} - \gamma_{j-\frac{1}{2}} G_{j-\frac{1}{2}} \right).
\end{aligned} \tag{17}$$

This matrix system is solved using a fast tridiagonal solver (Boris, 1976), and areas and velocities are calculated using,

$$\begin{aligned}
A_j^k &= \frac{\left(p_j^k - p_{eq}\right) \varepsilon_j A_{eq,j}^k}{p_{eq}} + A_{eq,j}^k \\
u_j^k &= \frac{A_j^k G_j}{8\pi\nu_j} - (p_j^k - p_{j-1}^k) \frac{A_j^k}{8\pi\nu_j \rho \delta S_j},
\end{aligned} \tag{18}$$

The procedure is iterated until the pressure solution converges.

Including the effects of the generalized acceleration term $G$ complicates the solution process significantly. Assume for now that the spatial gradients are small compared to the temporal gradients, and that there are no external body forces. Then

$$G \approx -\frac{\partial u}{\partial t}. \tag{19}$$

Applying this to equation 4, yields,

$$u = -\frac{A}{8\pi\nu} \frac{\partial u}{\partial t} - \frac{A}{8\pi\nu\rho} \frac{\partial p}{\partial S}. \tag{20}$$

Discretizing equation 20 yields,

$$u^k_{j+\frac{1}{2}} = -\frac{A^{k-\frac{1}{2}}_{j+\frac{1}{2}}(u^k_{j+\frac{1}{2}} - u^{k-1}_{j+\frac{1}{2}})}{8\pi\nu_{j+\frac{1}{2}}\delta t} - \frac{A^{k-\frac{1}{2}}_{j+\frac{1}{2}}(p^k_{j+1} - p^k_j)}{8\pi\nu_{j+\frac{1}{2}}\rho\delta S_{j+\frac{1}{2}}}, \tag{21}$$

and therefore, $u^k$ can be expressed as,

$$u^k_{j+\frac{1}{2}} = \frac{1}{1 + \frac{A^k_{j+\frac{1}{2}}}{8\pi\nu\delta t}} \left[ \frac{A^{k-\frac{1}{2}}_{j+\frac{1}{2}} u^{k-1}_{j+\frac{1}{2}}}{8\pi\nu_{j+\frac{1}{2}}\delta t} - \frac{A^{k-\frac{1}{2}}_{j+\frac{1}{2}}(p^k_{j+1} - p^k_j)}{8\pi\nu_{j+\frac{1}{2}}\rho\delta S_{j+\frac{1}{2}}} \right]. \tag{22}$$

We discretize equation 7 to obtain,

$$p^k_j - p^{k-1}_j = \frac{-p_{eq}\delta t}{\varepsilon A_{eq}\delta S_j} \left[ (uA)^{k-\frac{1}{2}}_{j+\frac{1}{2}} - (uA)^{k-\frac{1}{2}}_{j-\frac{1}{2}} \right]. \tag{23}$$

Substituting equation 22 into 23 yields,

$$p^k_j - p^{k-1}_j = -\beta_j\eta_{j+\frac{1}{2}} \left[ \gamma_{j+\frac{1}{2}} \frac{u^{k-1}_{j+\frac{1}{2}}}{\delta t} - \alpha_{j+\frac{1}{2}} \left( p^k_{j+1} - p^k_j \right) \right] + \beta_j\eta_{j-\frac{1}{2}} \left[ \gamma_{j-\frac{1}{2}} \frac{u^{k-1}_{j-\frac{1}{2}}}{\delta t} - \alpha_{j-\frac{1}{2}} \left( p^k_j - p^k_{j-1} \right) \right], \tag{24}$$

where,

$$\alpha_{j+\frac{1}{2}} = \frac{A^2_{j+\frac{1}{2}}}{8\pi\nu_{j+\frac{1}{2}}\rho\,\delta S_{j+\frac{1}{2}}}, \qquad \beta_j = \frac{\delta t\, p_{eq}}{\delta S_j \varepsilon_j A^{eq}_j}, \qquad \gamma_{j+\frac{1}{2}} = \frac{A^2_{j+\frac{1}{2}}}{8\pi\nu_{j+\frac{1}{2}}}, \qquad \eta_{j+\frac{1}{2}} = \left( 1 + \frac{A^k_{j+\frac{1}{2}}}{8\pi\nu\delta t} \right)^{-1}. \tag{25}$$

Rearranging terms yields

$$\left[ -\beta_j\eta_{j-\frac{1}{2}}\alpha_{j-\frac{1}{2}} \right] p^k_{j-1} + \left[ 1 + \beta_j \left( \eta_{j+\frac{1}{2}}\alpha_{j+\frac{1}{2}} - \eta_{j-\frac{1}{2}}\alpha_{j-\frac{1}{2}} \right) \right] p^k_j - \left[ \beta_j\eta_{j+\frac{1}{2}}\alpha_{j+\frac{1}{2}} \right] p^k_{j+1} = p^{k-1}_j - \beta_j \left( \eta_{j+\frac{1}{2}}\gamma_{j+\frac{1}{2}} \frac{u^{k-1}_{j+\frac{1}{2}}}{\delta t} - \eta_{j-\frac{1}{2}}\gamma_{j-\frac{1}{2}} \frac{u^{k-1}_{j-\frac{1}{2}}}{\delta t} \right). \tag{26}$$

Now, the set of vector coefficients have become,

$$\begin{aligned}
\mathbf{A}_j &= -\beta_j \eta_{j-\frac{1}{2}} \alpha_{j-\frac{1}{2}} \\
\mathbf{B}_j &= 1 + \beta_j (\eta_{j+\frac{1}{2}} \alpha_{j+\frac{1}{2}} + \eta_{j-\frac{1}{2}} \alpha_{j-\frac{1}{2}}) \\
\mathbf{C}_j &= -\beta_j \eta_{j+\frac{1}{2}} \alpha_{j+\frac{1}{2}} \\
\mathbf{D}_j &= \Delta p_j^{k-1} - \beta_j \left( \eta_{j+\frac{1}{2}} \gamma_{j+\frac{1}{2}} \frac{u_{j+\frac{1}{2}}^{k-1}}{\delta t} - \eta_{j-\frac{1}{2}} \gamma_{j-\frac{1}{2}} \frac{u_{j-\frac{1}{2}}^{k-1}}{\delta t} \right),
\end{aligned} \tag{27}$$

which are used in the tridiagonal system in equation 16.

This generalization of the method to $G \neq 0$ complicates the vector coefficients, but provides the ability to include body forces and temporal terms. Including large spatial gradients, however, requires further development and testing, and so is left for future research. A summary of the numerical method is given in table 1.

# 5 Results

In this section, we first present results for a baseline simulation that we use for comparison throughout the section. This simulation uses the simplest physical model, which assumes that the acceleration term is equal to zero ($G = 0$). The simulation was also performed using the $G = -\partial u/\partial t$ acceleration model, and they are compared to the $G = 0$ case in §5.2. Additionally, we present the model response to varying vessel elasticity (§5.3) and application of the generalized muscle contractions (§5.4).

For the cases presented here, the computational run times were on the order of 100 times faster than realtime (neglecting time needed for data output). Using the zero-acceleration model and a heartbeat of 1s, 12 heartbeats were computed in a CPU time of 60ms (5ms per heartbeat). When the nonzero-acceleration model was employed, 140 ms of CPU time were needed to compute 12 heartbeats (12 ms per heartbeat).

1. Initialize variables $\nu_j, \epsilon_j, A_{eq,j}$, $\Delta p_j$, $A_j$, $u_j$ at cell centers $j$.
2. Start time step loop. Current variables denoted by superscript $k$.
   (a) Define variable at previous timestep $k-1$, $(p^{k-1} = p^k, u^{k-1} = u^k, A^{k-1} = A^k)$
   (b) Apply equations 11 and 12 at locations of muscle contractions
      - Prescribed $A^k_{eq,j}$ in contracting cells, resultant $p^k_j$ calculated using equation 5
   (c) Activate valves if needed
      - At prescribed locations, check for adverse pressure gradient $(p_{jv} > (p_{jv-1} + 10.0))$
      - If so, decrease local area by 80%
      - If already decreased in previous timestep, set local area to 0
   (d) Activate distributed muscle contractions
      - Prescribed $A^k_{eq,j}$ in user-defined region, resulting $p^k_j$ calculated using equation 5
   (e) Solve for $p$ distribution
      - Calculate variables at interfaces $(A^k_{j-\frac{1}{2}}, u^k_{j-\frac{1}{2}})$
      - Set up tridiagonal system using equations in §4
      - Calculate $p^k_j$ using tridiagonal solver. Update $A^k_j$ and $u^k_j$ using equation 18
   (f) If $|p^k_j - p^{iter}_j| > p_{tol}$ (user-defined tolerance) anywhere, update $p^{iter}_j = p^k_j$ and returning to step 5.
   (g) If $|p^k_j - p^{iter}_j| < p_{tol}$ everywhere, end time loop. Return to 2.

Table 1: Numerical method summary

## 5.1 $G = 0$

The baseline simulation is initialized at $t = 0$ with zero velocity and an equilibrium pressure of 1.01 $p_{atm}$, which corresponds to a gauge pressure (above atmospheric) of 7.6 mmHg. Blood kinematic viscosity and density are taken as 0.05 $cm^2/s$ and 1.06 $g/cm^3$, respectively. Figure 2 shows the equilibrium area and weighted viscosity along the length of the system. The elasticity $\varepsilon$ is determined empirically and set to 1.0. The distributed skeletal muscle contraction model is not employed.

This simulation uses 100 computational cells to resolve a circulatory system that is 5 m in length with a total volume of 4.7 L, considered normal for an average adult human. The distribution of these cells is shown in figure 4. Each vascular tree uses 30 cells and begin six cells downstream of their respective ventricles (left ventricle for the systemic tree, and right ventricle for the pulmonary tree). The atria are located thirteen cells downstream of the vascular trees. Each chamber of the heart uses only one computational cell. Each of the four heart valves (mitral, aortic, tricuspid, and pulmonary) exists at the downstream interfaces of the atria and ventricles. There are four venous semi-lunar valves, two in each half of the circulatory loop. One valve is located two cells downstream of the vascular tree, and one is located 2 cells upstream of the atria.

Three sensors have been "inserted" at selected locations to describe the behavior of the arteries, capillaries, and veins. The approximate positions of the sensors are shown as green targets in figure 4. Arterial data is obtained at $S = 0.3$ m, which is two computational cells downstream of the right ventricle, and four cells upstream of the systemic vascular tree. The capillary data sensor is positioned at the point of largest area expansion ($S(X_{mid}) = 1.25$ m), and the venous data sensor is located 5 computational cells downstream of the systemic vascular tree at $S = 2.25$ m.

Profiles of the varying cross-sectional area, gauge pressure, and velocity at the three sensor locations are shown in figures 5(a) and 5(b). They are shown for the very first cycle of the simulation. When the data were phase-averaged over the first 25 heartbeats, the largest standard deviation in pressure, among all locations, was only 0.0057. Area and pressure profiles are qualitatively very similar to each other because these quantities are linearly related through the equation of state (equation 5). The pressure at all three locations begins at equilibrium (7.6 mmHg).

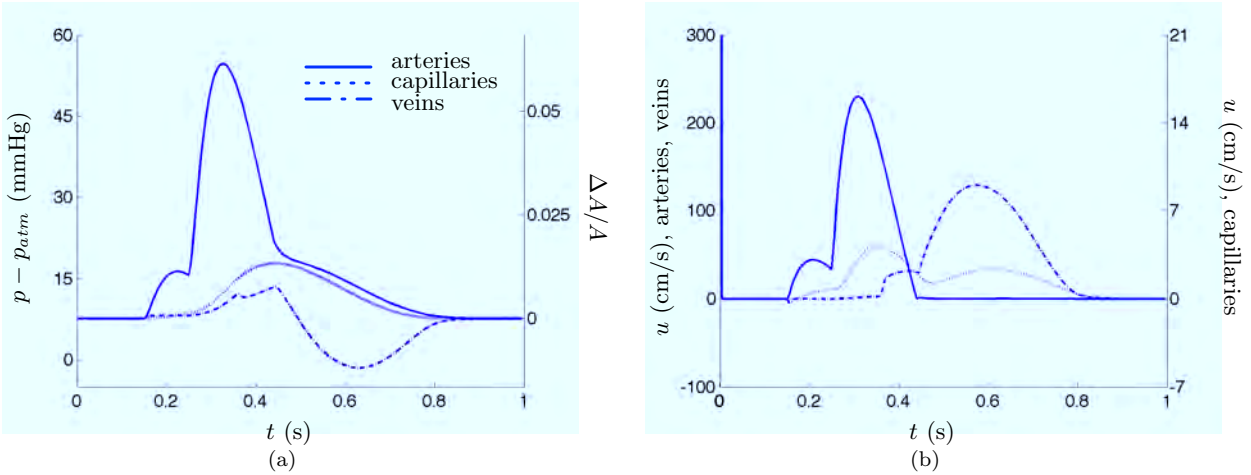


Figure 5: Time resolved plots of (a) pressure, area, and (b) velocity at three locations in the vasculature. $G = 0$.

Figure 3(a) shows that the atria begin to contract at 0.15s, causing the arterial pressure and area to increase quickly (solid line). The pressure in the capillaries (dashed) and veins (dash-dot) begin increasing more slowly. At 0.25s, the ventricles begin to contract, while at 0.36s the atria have begun to relax and expand slowly. This atria expansion causes a brief drop in the venous pressure at 0.36, but the increasing ventricle contraction increases the pressure until 0.45s. The ventricles begin to expand at 0.44s, but the closing of the aortic valve keeps the pressure from continuing to drop so quickly in the arteries. After this time, the expansion of both chambers causes a low pressure in the heart, but the favorable gradient keeps the mitral and venous semi-lunar valves open, and hence the pressure in the veins drops to below the equilibrium pressure. It then increases slowly back to $p_{eq}$ at 0.9s, after both chambers of the heart have relaxed back to the default equilibrium area. At the same time, the pressure in the arteries and capillaries decreases smoothly back to the equilibrium pressure.

There is a precipitous drop in peak pressure between the arteries and the capillaries. In the veins, pressure decreases further, and even falls below the equilibrium pressure. Guyton & Hall (2000) reports that normal mean pressures are 100 mmHg in the arteries, 20 mmHg in the capillaries, and only 5 mmHg in the veins. The curves presented here thus under-predict the arterial and capillary pressures and over-predict the venous pressures. This indicates that a more refined distribution of equilibrium pressure and actuation of the valve models is needed and gives some indication of future work.

Time-resolved velocities are shown in figure 5(b). Arterial velocities (solid line) increase as the atria begin to contract at 0.15s. As the rate of atria contraction slows, the velocity in the arteries falls slightly, but remains positive. Velocity in the capillaries (dashed), which is scaled using the ordinate on the right, increases similarly at 0.15s, although at a slower rate. Both velocities increase greatly as the ventricle starts to contract at 0.25s Arterial velocity peaks at 0.31s and capillary pressure peaks shortly after at 0.35s. As the atria begin to contract, there is a brief negative velocity in the veins (dash-dot), but the associated adverse pressure gradient is detected and mitigated quickly by the semilunar valves in the veins. The velocity in the veins is relatively low during the ventricle contraction.

As the atria expand after 0.34s, the velocity in the veins is small and positive, but the venous velocity increases greatly at 0.44s, after which all chambers of the heart are expanding. This creates the low pressure observed in figure 5(a), drawing blood through the veins into the heart. In the capillaries, the velocity has two peaks, each lining up with the peak in the arterial velocity, associated with the contraction of the heart, and the venous velocity, which occurs later with the heart expansion. In other words, flow through the capillaries increases when it is both pushed from the arteries and pulled from the veins. Peak velocities in the capillaries, however, are much lower that in the arteries and veins. This is a result of the increased cross-sectional area in the vascular trees.

Time-averaged velocities are compared with data from Charm & Kurland (1974) in table 2 and average values are on the same order of magnitude. The main discrepancy is the mean velocities of the arteries and veins. In the reference data, the mean venous velocity is approximately half the mean arterial value, while for our baseline simulation, the mean venous velocity is the same or slightly larger than mean arterial velocity. Figure 5(b) shows, however, that the maximum velocity in the arteries is considerably larger than the maximum venous velocity. The ratio of maximum velocities ($230/129 = 1.8$) is about the same as the ratio of mean velocities from the reference data ($45/24 = 1.9$).

| | $\mathbf{G = 0}$ | | $\mathbf{G = -\partial u/\partial t}$ | | **C & K** |
|---|---|---|---|---|---|
| | $\bar{\mathbf{u}}$ | $\mathbf{u_{max}}$ | $\bar{\mathbf{u}}$ | $\mathbf{u_{max}}$ | $\bar{\mathbf{u}}$ |
| **Arteries** | 30.6 | 229.7 | 49.5 | 260.8 | 45 |
| **Capillaries** | 1.2 | 4.1 | 2.0 | 8.3 | 1.7 |
| **Veins** | 32.1 | 128.7 | 53.0 | 173.4 | 24 |

Table 2: Mean velocity comparison with Charm & Kurland (1974). All velocities are in cm/s.

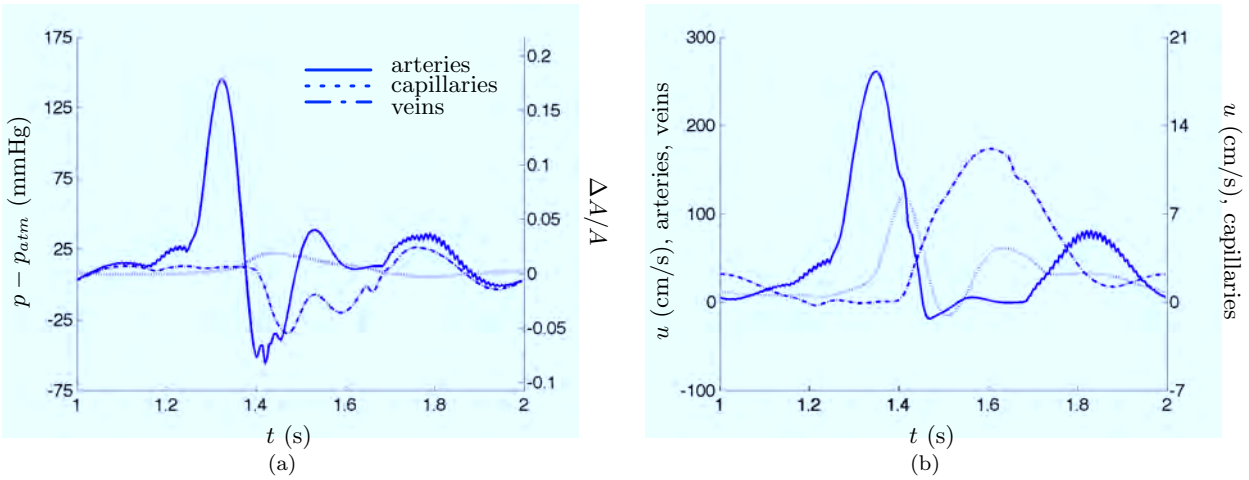


Figure 6: Time resolved plots of (a) pressure, area, and (b) velocity at three locations in the vasculature. Results are from a simulation using the acceleration model ($G = -\partial u/\partial t$).

## 5.2 Nonzero-acceleration model

Using the same input parameters and computational configuration, a simulation was also calculated using the nonzero-acceleration model described in §4. Here, the acceleration term $G$ is modeled as $G = -\partial u/\partial t$. Profiles of area, pressure, and velocity are obtained at the same three "sensor" locations and shown in figure 6. These profiles are from the second heartbeat calculated (1s $< t <$ 2 s). Phase-averaging over 24 heartbeats, from the second to the twenty-fifth, yielded a maxiumum standard deviation in pressure, among all locations, of only 0.007. The first heartbeat deviates from the subsequent cycles at the initial condition ($p(0) = p_{eq}$).

Peak pressures in the arteries are much greater than those in the capillaries, which is similar to the result for $G = 0$. Also, the pressure in the veins is less than the equilibrium pressure for most of the heartbeat. There are significant differences, however, in both the magnitude of the peak pressures, and the qualitative characteristics of the time-varying profiles.

At the beginning of a heartbeat, the pressures in both the arteries (solid line) and the veins (dash-dot) are increasing slightly, and a small magnitude, high frequency oscillation is present in the arterial pressure. Both of these phenomena are due to the effects of the previous heartbeat. When the atria begin to contract at 1.15s, the arterial pressure increases to a second peak. As the ventricles begin to contract at 1.25s, the arterial pressure increases more quickly, and reaches its maximum at 1.33s, the same phase at which peak arterial pressure is reached when using the zero-acceleration model. The arterial pressure from the acceleration model decreases more quickly, however, dropping below the equilibrium pressure at 1.38s while the ventricle is still contracting. At 1.34s, the atria begin to expand and the pressure in the veins drops below the equilibrium pressure. The pressure in the capillaries (dashed) increases slowly to its maximum at 1.43s, at which time the ventricles stop contracting and begin to expand.

As the ventricles approach maximum contraction, the mitral and aortic valves react to the changing pressure distribution in the heart, and their opening and closing cause the fluctuation in the arterial pressures observed from 1.4s to 1.43s. A longer time-scale oscillation is observed in both the arterial and venous pressures from 1.45s until the end of the heartbeat at 2s, which is caused by the inclusion of the acceleration model, as expressed in equation 9. The rate of change of pressure depends not only on the curvature of the pressure distribution, but on the distribution of the acceleration. As observed in figure 5, the pressure and velocity are not always in phase, and therefore the inclusion of the this term can induce an oscillation in those regions where the fluid acceleration is large, such as the arteries and veins.

At 1.68s, the high-frequency oscillation of the arterial pressure begins, which was also observed near the beginning of the heartbeat. This is due to the high sensitivity of both the mitral and aortic valves, which open or close at each timestep because the pressures in the heart chambers and the aorta are roughly equal. If the valves are designed to only close when the downstream pressure is more than 7.5 mmHg larger than that upsteam of the valve, this chattering of the arterial pressure signal is eliminated, as shown in figure 7(a). The pressure profiles for the two different valve sensitivities are qualitatively very similar. Using the less sensitive valves that close at the higher adverse pressure, there is a period of increased venous pressure from 1.2s to 1.34s. This is a result of the venous semi-lunar valve downstream of the sensor location not activating while the atria contract. In fact, using the less sensitive valve model, the venous semi-lunar valves are not

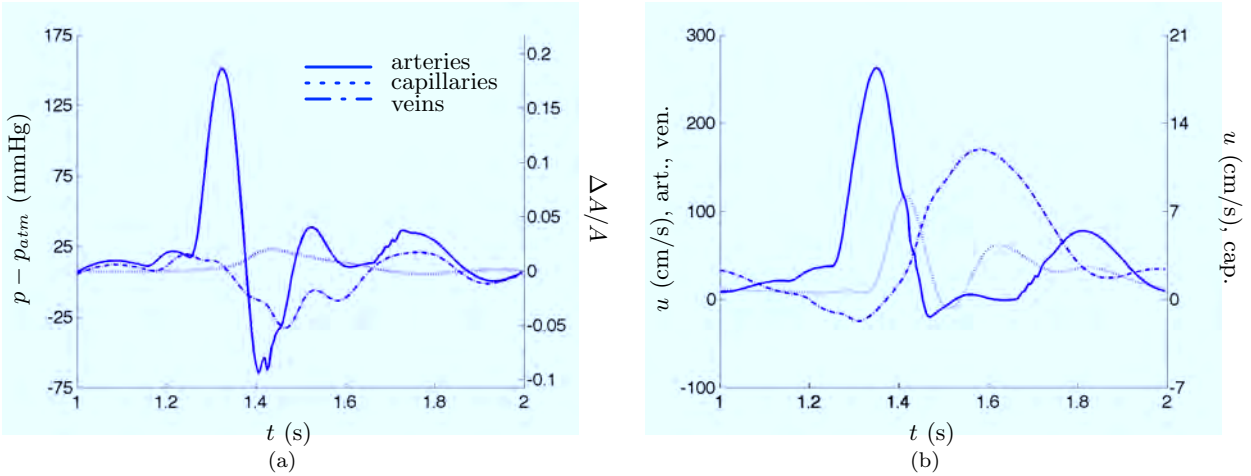


Figure 7: Time resolved plots of (a) pressure, area, and (b) velocity at three locations in the vasculature. Results are from a simulation using the acceleration model ($G = -\partial u/\partial t$). In this model, valves only close when the downstream pressure is more that 7.5 mmHg larger than the upstream pressure.

activated during the entire heartbeat.

Comparing the results of the two different acceleration models, a significant difference exists in the magnitudes of the arterial pressure profiles. The peak arterial pressure using the zero-acceleration model was 54 mmHg, while including the acceleration model more than doubles it to 147 mmHg. This is attributed to the relatively high fluid acceleration in the arteries, which amplifies the maximum pressure at 1.33s and the minimum pressure at 1.4s. Alternatively, in the capillaries where there is relatively little fluid acceleration, the peak pressure only increases from 17.8 mmHg in the zero-acceleration case to 22.1 mmHg here. In the veins, the acceleration model decreases the minimum pressure to 35 mmHg below atmospheric, whereas it was only 1.5 mmHg below atmospheric when using the zero-acceleration model.

The velocity profiles obtained using the $G = -\partial u/\partial t$ acceleration model differ from the zero acceleration case similarly to the way the pressure profiles do, as seen in figure 6(b). At the beginning of the heartbeat, the velocities at all three data sensor locations are non-zero and still oscillating from the previous heartbeat. The arterial velocity begins to increase more significantly at 1.6s, shortly after the atria begin to contract. At 1.25s, when the ventricles begin to contract, the arterial velocity increases at an even greater rate and the high frequency oscillation attributed to the mitral and aortic valve sensitivities is eliminated. At this point in time, the velocity in the capillaries also begins to increase slowly. The arterial velocity peaks at

1.35s, and the capillary velocity peaks later, at 1.41s. When the ventricles begin to expand at 1.45s, the oscillating pressure observed in figure 6(a) creates a period of low-amplitude reversed flow in the arteries and the capillaries.

The venous velocity begins to increase at 1.4s when the atria begin to expand. It peaks at 1.6s, and shortly after, at 1.63s, the capillary velocity peaks a second time. This double peak in capillary velocity is similar to that the zero-acceleration case. Due to the oscillating pressure that occurs in the arteries near the end of the heartbeat, there is an additional period of positive arterial velocity from 1.69s to 2s, during which the valve sensitivity creates the high frequency oscillation in the arterial velocity profile. As seen in figure 7(b), this chattering is again eliminated by using valves of lower sensitivity, which are not activated until the downstream pressure exceeds the upstream pressure by more than 7.5 mmHg. Because the semi-lunar valves are never activated in this case, as previously mentioned, a period of reversed flow occurs in the veins from 1.2s until 1.37.

In table 2, mean and maximum velocities at the three sensor data locations are also included for the acceleration model case. As expected, inclusion of the acceleration model increases the mean and maximum velocities at all three locations, just as it was observed to increase the oscillating pressure magnitudes. The mean venous velocity is slightly greater than the arterial velocity, similar to the zero-acceleration case, but the ratio of arterial to venous maximum velocities, however, is lower ($261/173 = 1.5$).

### 5.3 Effects of system elasticity

After establishing the baseline distributions of pressure, area, and velocity through the model vasculature, we can begin to explore the effects of varying input parameters and applying additional forcing. In figure 8, we show the time-resolved pressure in the arteries and capillaries for three values of rigidity, simulated using both the zero acceleration and the ($G = -\partial u/\partial t$) model. An increase in rigidity is applied as a decrease in the elasticity ($\varepsilon$) in the equation of state throughout the vasculature. Using the $G = 0$ model, a 25% decrease in elasticity cause a 6% increase in peak pressure in the arteries and a 15% increase in peak capillary pressure. Halving the elasticity caused an 19% increase in peak arterial pressure and a 58% increase in the

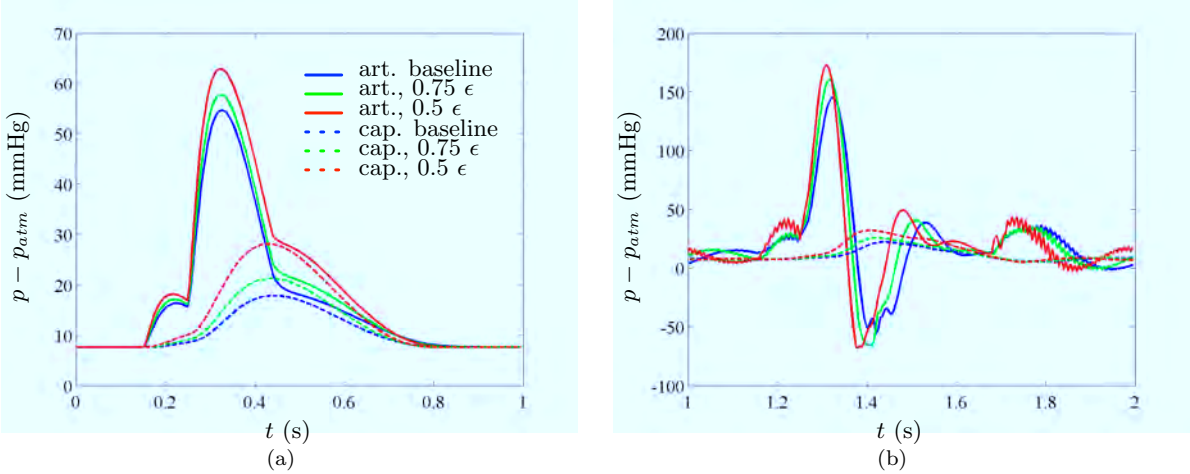


Figure 8: Effects of vasculature rigidity (a) $G = 0$ and (b) $G = -\partial u/\partial t$

| | $\mathbf{G = 0}$ | | | $\mathbf{G = -\partial u/\partial t}$ | | |
|---|---|---|---|---|---|---|
| | **100**% $\varepsilon$ | **75**% $\varepsilon$ | **50**% $\varepsilon$ | **100**% $\varepsilon$ | **75**% $\varepsilon$ | **50**% $\varepsilon$ |
| **Arteries** | 54.6 | 57.8 (+6%) | 62.9 (+15%) | 147.3 | 160.3 (+9%) | 174.2 (+18%) |
| **Capillaries** | 17.8 | 21.2 (+19%) | 28.1 (+58%) | 22.1 | 25.7 (+16%) | 32.1 (+45%) |

Table 3: Peak pressures (in mmHg) for different elasticities in the two models, and the percentage increase over the baseline value.

capillaries. Similar increases were also seen when using the $G \neq 0$ model, and these are summarized in table 3. A 25% decrease in elasticity cause a 9% increase in peak pressure in the arteries and a 16% increase in peak capillary pressure, while a 50% decrease in elasticity caused an 18% increase in peak arterial pressure and a 45% increase in the capillaries.

When including the acceleration model, another effect of the increased rigidity is shown in in figure 8(b). As rigidity increases, not only do the peak pressures increase over the baseline case, they also occur slightly earlier. The loss of flexibility advances the dynamic response of the system. Furthermore, from 1.37s to 1.46s, the increased rigidity appears to mitigate some of the heart valve chattering effects because the arterial pressure profile is smoother. Future work will investigate the effects of varying the elasticity along the vasculature and the system sensitivity.

### 5.4 Effects of distributed muscle contractions

Distributed muscle contractions, as described in §3, were applied to simulations using both acceleration models, and the results were evaluated by analyzing time-averaged flow velocities in the veins. It is at this location where the physical benefit of these contractions, represented as an velocity increase, are considered important to help drive blood back towards the heart despite the relatively low venous pressures.

Test cases were run for muscle contractions at frequencies in the range 0.5 Hz $< f_m <$ 2.0 Hz and maximum amplitudes in the range $0.005 < \Delta A_m/A < 0.02$. A summary of the muscle contraction effects are plotted in figure 9, where mean venous blood flow velocities are shown for four contraction amplitudes at four contraction frequencies. These mean velocities were averaged over six heartbearts to ensure than an integer number of muscle contractions were included in the timeseries for all frequencies. In both acceleration model cases, increasing amplitude increases the blood flow benefit at all but one contraction frequency. At 1 Hz, there is no benefit to venous flow according to the zero-acceleration model, and when using the nonzero-acceleration model, muscle contractions at this frequency actually inhibit venous flow. This is assumed to be a result of contracting in phase with the heart pumping, effectively working against it.

For the cases studied here, the lowest frequency of muscle contractions (0.5 Hz) created the greatest venous flow benefit for both acceleration models at almost all amplitudes. Future work will include a phase shift between the muscle contractions and heart pumping in order to better understand how to optimize venous blood flow.

## 6 Discussion

A new low-dimensional numerical model of the human circulatory system is introduced, consisting of a one-dimensional axisymmetric circular elastic pipe with periodic boundary conditions. Computational runtimes were on the order of 100 times faster than realtime. Five liters is considered a normal volume for an adult human circulatory system (Guyton & Hall, 2000), and the model presented here has a pipe length of 5m and a cross-sectional area distribution that yields a total circuit volume of 4.7 L. The fluid forcing is accomplished

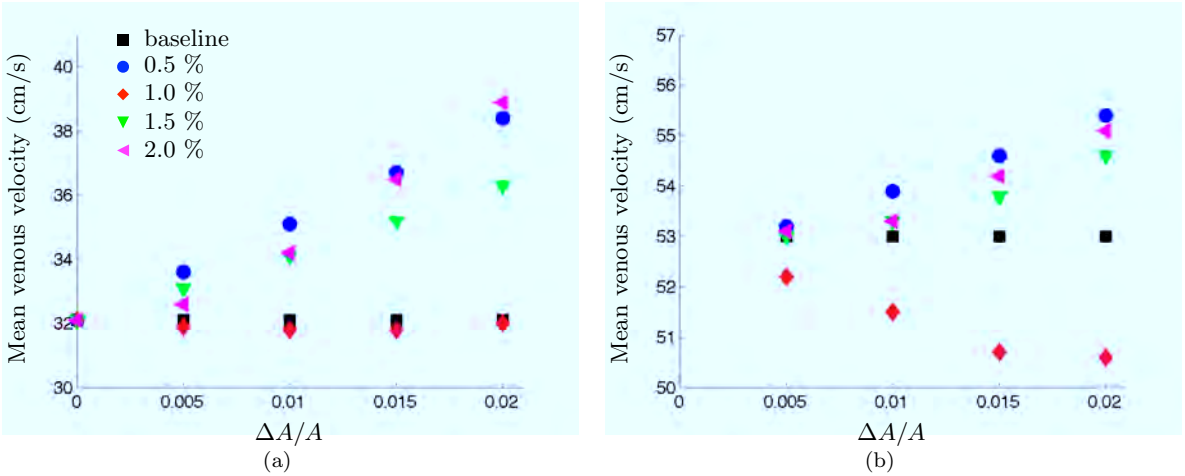


Figure 9: Mean venous flow velocities for a range of contraction amplitudes and frequencies. (a) $G = 0$ and (b) $G = -\partial u/\partial t$

through an effective contraction and relaxation of the local area near the heart and is aided by a set of model valves in the heart and along the vascular tree to prevent expected backflow.

This circulatory system model performs reasonably well and predicts some large scale dynamic quantities. The magnitude of pressure oscillations is approximately correct and, as expected, it is largest in the arteries and decreases precipitously in the capillary region. Large pressure oscillations were also observed in the veins due to the low pressures created by the left atrium expansion. Mean velocities at points in the arteries, capillaries, and the veins compared well with reference data from Charm & Kurland (1974) (table 2). One main discrepancy is the over-prediction of mean velocity in the veins, which results from the large low-pressure oscillations. Future model development that resolves the correct venous pressure signature should also decrease the local mean velocity.

The model was also applied using a modified set of equations that included the pressure drop caused by a fluid acceleration term. When the acceleration effects are included, the time-resolved pressures exhibit a larger amplitude in the the arteries and veins, where the fluid acceleration is expected to be high. Also, in these regions the pressure oscillates at a frequency that is higher than the heartbeat due to the nonlinear feedback of the fluid acceleration into the model. This formulation also makes it more difficult to predict the effects that improvements to the model geometry and characteristics of the system model will have on

the nonzero-acceleration simulations.

When using the nonzero-acceleration model, a very high-frequency pressure oscillation also occurs near the beginning and end of the heartbeat, when the fluid is decelerating and the pressure in and around the heart chambers is fairly constant. The chattering of the pressure (and velocity) comes from the rapid opening and closing of the mitral and aortic valves. If the valves are calibrated to only close at a larger adverse pressure gradient, this chattering is eliminated. Future work will refine the implementation of these valves so that they perform more smoothly and realistically.

Changes to the model parameters and inputs from the baseline simulation produce realistic responses in the circulatory model. An increase in vascular rigidity by 25% increases the arterial pressure maximum in the $G = 0$ ($G \neq 0$) simulation by 6% (9%). Doubling the rigidity increased the maximum arterial pressure by 15% (18%). The application of distributed muscle contractions, used to model the added pumping from skeletal muscle contractions, was shown to increase the mean venous velocities in the model. At the largest distributed muscle contraction, with maximum amplitude of 2%, there is an increase of 20% in the mean venous velocity using the zero-acceleration model, and 5% using the nonzero-acceleration model.

There are several geometric and mechanical characteristics of the current model that need to be refined as development continues, despite the current qualitative similarities on the macro length and time scales. The relative cross-sectional areas and lengths of the arteries, capillaries, and veins are currently defined heuristically, so that the total volume and length are physiologically realistic. Also, the two halves of the circulatory loop (systemic and pulmonary) are symmetric, even though it is known that this is not the case in human physiology. The physical pulmonary circuit is considerably shorter and offers less resistance to the output of the right ventricle than the systemic circuit offers to the left ventricle. Future development of the model will focus on the realistic calibration of the quantities such as segment length, area, distribution of the weighted viscosity and elasticity, and valve representation.

With respect to the model of the actuated heart chambers, it is not in the scope of this work to correctly capture the complex three-dimensional dynamics. Rather, we will use calibrated phenomenologies to capture the results of experiments and more detailed simulations. For this model, it is important to

recreate a physiologically realistic cardiac output, and future work to refine the model of heart pumping will focus on replicating the quantity of fluid pumped, but not necessarily on geometrically matching the physical heart.

A primary concern about the large-scale dynamic behavior of the model is that it does not yet correctly capture a high mean pressure in the arteries. In reality, the high pressure created by the contraction of the heart keeps the aorta and the large arteries at a pressure near 100 mmHg above atmospheric. We have so far attempted to address this issue in two ways. First, the local equilibrium area was set to be greater in the large arteries, which initiated a larger arterial pressure, but this relaxes to the lower equilibrium pressure within two heartbeats. Consequently, the local pressure is much lower than the equilibrium pressure in the arteries, causing a significant decrease in the local area.

A second approach to correct this discrepancy was to increase the weighted viscosity in the capillary region. This not only drives up the pressure in the arteries as the heart pumps, but at high enough values, the arterial pressure relaxes to equilibrium at a rate slower than the heart rate. The arterial pressure then oscillates around a higher mean, as desired. This approach, however, significantly decreases the low pressure on the venous end of the vasculature. The enhanced resistance in the capillaries achieved by a higher viscosity does increase the arterial pressure, but at the cost of unrealistically low venous pressure and high venous velocities. Further research, augmented with additional expertise, is needed to resolve this issue.

In addition to the continued improvement of this circulation model, other future work is planned to expand the scope of this project. Currently, a similar formulation is being used to develop a model of the respiratory system. These two independent models will then be coupled together through a model of the respiration process, involving the transport of gases ($O_2$ and $CO_2$) across the blood gas barrier. We also plan to develop an independent fluid dynamic model of the lymphatic system, although a new formulation may be needed to appropriately capture its diffusion-dominated dynamics. The lymph (interstitial fluid) comes from a slow "leak" of material out of circulatory system, and the lymphatic system returns it at the venous ends of the systemic vasculature. This process provides another natural coupling between the circulatory and lymphatic system models.

The refinement of the circulatory system model, the development of independent respiratory and lymphatic models, and the careful coupling among them will occur simultaneously. It is as yet too soon to state that the interaction of the relatively simple models will be able to recreate, on some level, the intricate and nonlinear behavior of the human body as a whole, but the progress is promising.


### Acknowledgments

This work was supported, in part, by the NRC Research Associate Program, the Office of Naval Research through NRL, and DTRA-JSTO for Chemical and Biological Defense.


## References


Bassingthwaighte, James B. 2000 Strategies for the physiome project. *Annals of Biomedical Engineering* **28**, 1043–1058.

Boris, Jay P. 1976 Vectorized tridiagonal solvers. NRL Memorandum Report 3408. Naval Research Laboratory, Washington, DC.

Charm, Stanley E. & Kurland, George S. 1974 *Blood Flow and Microcirculation*. New York: John Wiley & Sons.

Green, Melissa A., Kaplan, Carolyn R., Oran, Elaine S. & Boris, Jay P. 21-23 November, 2010 A dynamic model o f human physiology. In *63rd Annual Meeting of the American Physical Society Divison of Fluid Dynamics*. Long Beach, CA.

Grinberg, Leopold, Anor, Tomer, Cheever, Elizabeth, Madsen, Joseph R. & Karniadakis, George Em 2009 Simulation of the human intracranial arterial tree. *Philosophical Transactions of the Royal Society A* **367**, 2371–2386.

Grinberg, Leopold, Cheever, Elizabeth, Anor, Tomer, Madsen, Joseph R. & Karniadakisrniadakis, George Em 2011 Modeling blood flow circulation in intracranial arterial networks: A comparative 3d/1d simulation study. *Annals of Biomedical Engineering* **39** (1), 297–309.

Guyton, Arthur C. & Hall, John E. 2000 *Textbook of Medical Physiology*. W. B. Saunders Company.

Neil, Maxwell Lewis & Bassingthwaighte, James B. 2007 Subject-specific model estimation of cardiac output and blood volume during hemorrhage. *Cardiovascular Engineering* **7**, 97–120.

Noordergraaf, Abraham, Verdouw, Pieter D. & Boom, Herman B. K. 1963 The use of an analog computer in a circulation model. *Progress in Cardiovascular Diseases* **5** (5), 419–439.

Olufsen, Mette S. 1999 Structured tree outflow condition for blood flow in larger systemic arteries. *American Journal of Physiology - Heart and Circulatory Physiology* **276**, 257–268.

Olufsen, Mette S., Peskin, Charles S., Kim, Won Yong, Pedersen, Erik M., Nadim, Ali & Larsen, Jesper 2000 Numerical simulation and experimental validation of blood flow in arteries with structure-tree outflow conditions. *Annals of Biomedical Engineering* **28**, 1281–1299.

Schaaf, Bernard W. & Abbrecht, Peter H. 1972 Digital computer simulation of human systemic arterial pulse wave transmission: A nonlinear model. *Journal of Biomechanics* **5**, 345–364.

Sheng, C., Sarwal, S. N., Watts, K. C. & Marble, A. E. 1995 Computational simulation of blood flow in human systemic circulation incorporating an external force field. *Medical & Biological Engineering & Computing* **33**, 8–17.

Snyder, M. F., Rideout, V. C. & Hillestad, R. J. 1968 Computer modeling of the human systemic arterial tree. *Journal of Biomechanics* **1**, 341–353.

Staples, Anne E., Oran, Elaine S., Boris, Jay P., Kaplan, Carolyn R. & Kailasanath, K. 18-20 November, 2007 The pulsed flow algorithm applied to coupled respiratory and circulatory systems. In *60th Annual Meeting of the American Physical Society Divison of Fluid Dynamics*. Salt Lake City, UT.

Steele, Brooke N., Wan, Jing, Ku, Joy P., Hughes, Thomas J. R. & Taylor, Charles A. 2003 In vivo validation of a one-dimensional finite-element method for predicting blood flow in cardiovascular bypass grafts. *IEEE Transactions on Biomedical Engineering* **50** (6), 649–656.

Vignon-Clementel, Irene E., Figueroa, C. Alberto, Jansen, Kenneth E. & Taylor, Charles A. 2006 Outflow boundary conditions for three-dimensional finite element modeling of blood flow and pressure in arteries. *Computational Methods in Applied Mechanical Engineering* **195**, 3776–3796.

Wan, Jing, Steele, Brooke N., Spicer, Sean A., Strohband, Sven, Feijoo, Gonzalo R., Hughes, Thomas J. R. & Taylor, Charles A. 2002 A one-dimensional finite element method for simulation-based medical planning for cardiovascular disease. *Computer Methods in Biomechanics and Biomedical Engineering* **5** (3), 195–206.

Westerhof, Nicolaas, Bosman, Frederik, de Vries, Cornelis J. & Noordergraaf, Abraham 1969 Analog studies of the human systemic arterial tree. *Journal of Biomechanics* **2**, 121–143.

Womersley, J. R. 1955 Method for the calculation of velocity, rate of flow and viscous drag in arteries when the pressure gradient is known. *Journal of Physiology* **127**, 553–563.

Womersley, J. R. 1957 Oscillatory flow in arteries: the constrained elastic tube as a model of arterial flow and pulse transmission. *Physics in Medicine and Biology* **2**, 178–187.

Zagzoule, Mokhtar & Marc-Vergnes, Jean-Pierre 1986 A global mathematical model of the cerebral circulation in man. *Journal of Biomechanics* **19** (12), 1015–1022.